ACS Energy LETTERS

http://pubs.acs.org/journal/aelccp

Pathways to High-Power-Density Redox Flow Batteries

Kiana Amini, Amit N. Shocron, Matthew E. Suss,* and Michael J. Aziz*

Cite This: *ACS Energy Lett.* 2023, 8, 3526–3535

ABSTRACT: **Redox flow batteries (RFBs) promise to fill a crucial missing link in the energy transition: inexpensive and widely deployable grid and industrial-scale energy storage for intermittent renewable electricity. While numerous lab-scale and demonstration-scale RFBs have been delivered, widespread commercial deployment is still limited by high electrolyte, stack, and balance of plant capital costs. Increasing the power density of RFBs is correlated with lower stack costs, primarily because the area needed for expensive electrode and membrane components to reach a target power density is reduced. In the present contribution, we summarize the areal power densities reported for lab-scale RFBs, critically evaluate major pathways employed for power optimization, and identify opportunities for developing yet-higher power density systems.**

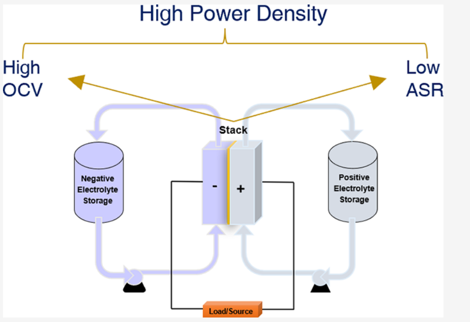

The deployment of grid-integrated renewable sources of energy, such as solar and wind power, has accelerated markedly in recent years, with the fastest growth reported in 2022, constituting 27.3% of the total generating capacity in the United States, with wind capacity increasing 56.6% and solar capacity growing 92.2% above the forecasts made in 2019.[1−3] While such renewable sources are leading clean and sustainable options, their intermittent nature makes them unreliable sources for large-scale power production. Clean, reliable, and cost-effective energy storage technologies are needed to effectively time-shift energy production to better match supply and demand.

Redox flow batteries (RFBs) constitute an attractive renewable energy storage technology which, unlike Li ion batteries, can be scaled up with independent control of the system's energy and power capacities. In RFBs, the output power (kW) is controlled by the active area of the electrodes and membrane, whereas the energy capacity (kWh) is set by the volume of the electrolyte and the concentration of the electroactive species. This spatial decoupling of energy and power can be leveraged to easily create discharge durations from hours to days, while typical Li ion installations are limited to up to 5-h discharge duration.[4] One major challenge impeding the successful and ubiquitous deployment of RFBs is their high capital cost. A recent assessment of current and future cost estimations of all-vanadium RFBs (VRFBs), which are the farthest along the commercialization pathway, estimates a current electrolyte and stack cost of \$280/kWh for a 1 MW VRFB with 4-h discharge duration. This is projected to drop to \$230/kWh by 2030.[5] Because widespread, cost-effective deployment for price arbitrage on the electrical grid requires installed costs closer to \$100/kWh, projected cost reductions are insufficient for this objective.[6] RFBs with higher power density should exhibit reduced capital cost because fewer cells would be required for the target power capacity. A review of reported prices for VRFB cell stacks shows that battery stacks alone have prices with a median of \$130/kWh for an energy-to-power ratio of 8 h,[7] already far from the target prices. Thus, stack cost reductions are necessary, and the most likely direction for pursuing such cost reductions is increasing power density.

In the present contribution, we examine the areal power density performance of lab-scale RFBs with varying chemistries and cell architectures. We find that only six chemistries have enabled cells attaining >1 $W \cdot cm^{-2}$ power density, and solely one with >2 $W \cdot cm^{-2}$, a surprising result which motivates this work. Major power optimization strategies employed in the literature are identified and critically assessed, with implications for attaining yet-higher power densities discussed. After an overview of the current state of the field (section 1), the discussion is organized into four parts. First, section 2 critically evaluates low open-circuit voltage (OCV) batteries, cells with <1.3 V OCV, that achieve high power densities of >1 $W \cdot cm^{-2}$ via cell resistance optimization (top-left region of Figure 1). The next part (section 3) examines chemistries and cells relying largely on high OCVs to attain large power output (top-right region of

Received: May 26, 2023
Accepted: July 17, 2023

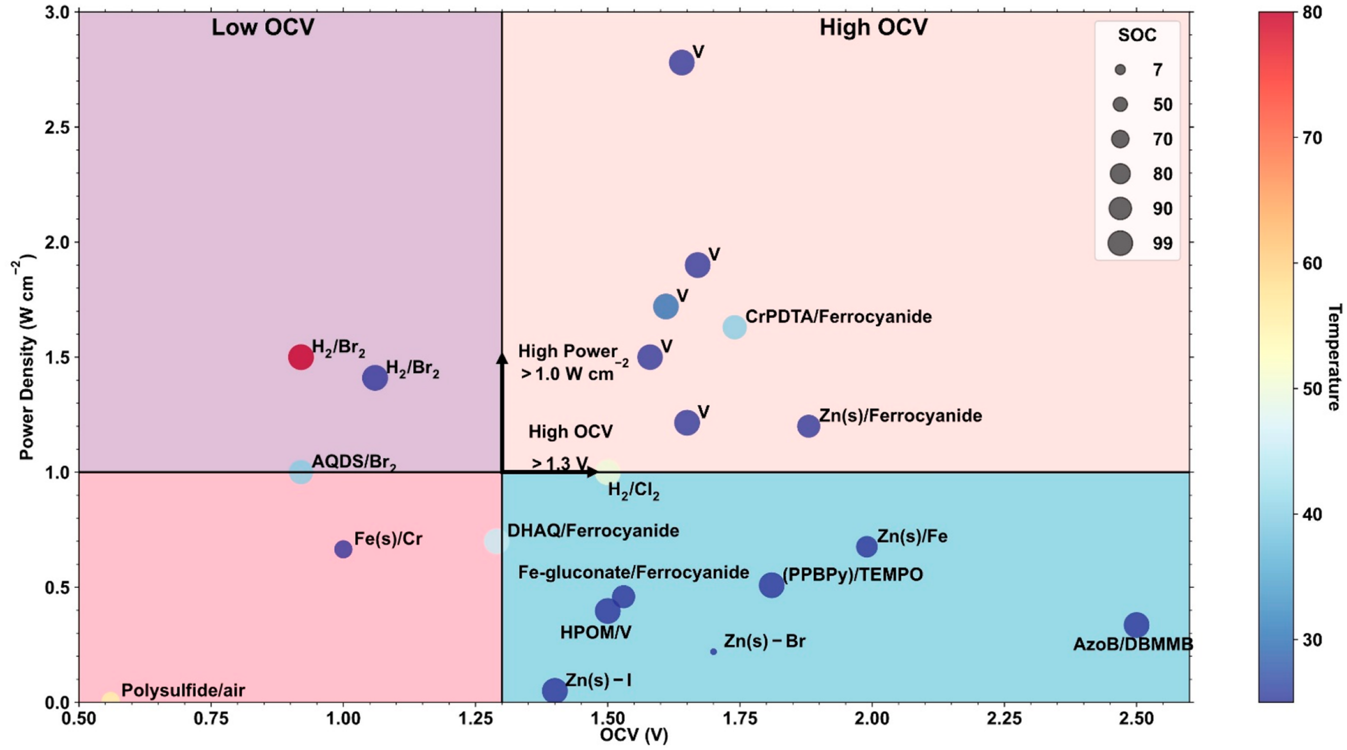

Figure 1. Power density versus open-circuit voltage of selected chemistries reported in the literature.[8−28] The size and color of the circle next to each chemistry represent the state of the charge and the temperature employed, respectively.

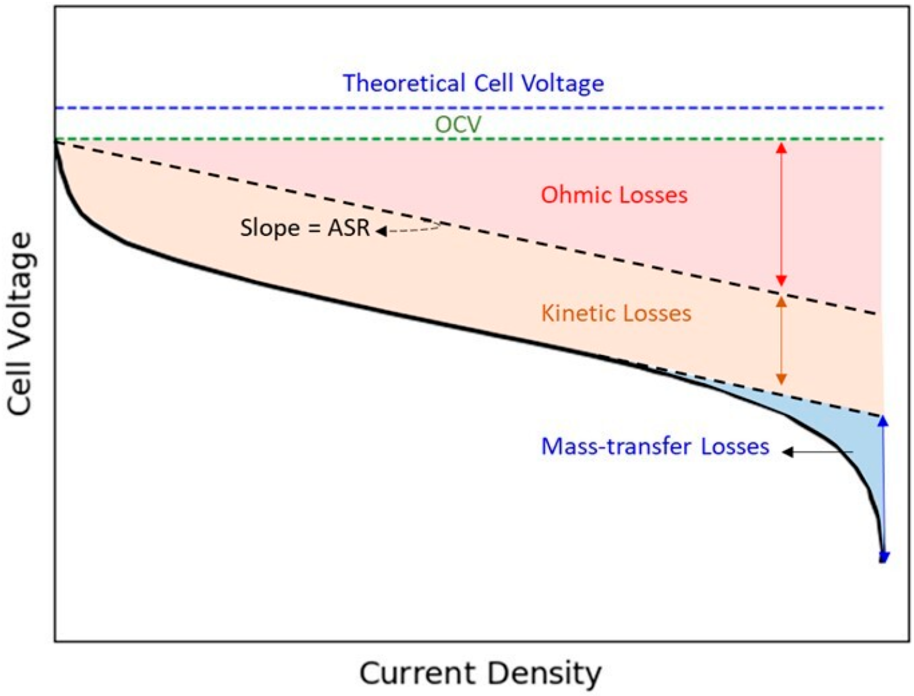

Figure 2. Typical flow battery polarization curve during discharging (voltage versus discharge current density) with dissected contributions of ohmic, kinetic, and mass-transfer losses.

Figure 1). This section additionally discusses chemistries with high OCVs which have not yet demonstrated high power densities (bottom-right region in Figure 1). The third part (section 4) critically evaluates a VRFB with the highest power density ever reported for any redox flow battery. The fourth part (section 5) discusses conditions where mass-transfer losses can become important when considering the power output of the battery.

1. CURRENT STATE OF THE FIELD

Figure 1 presents a snapshot of measured maximum power density versus open-circuit voltage for several flow battery

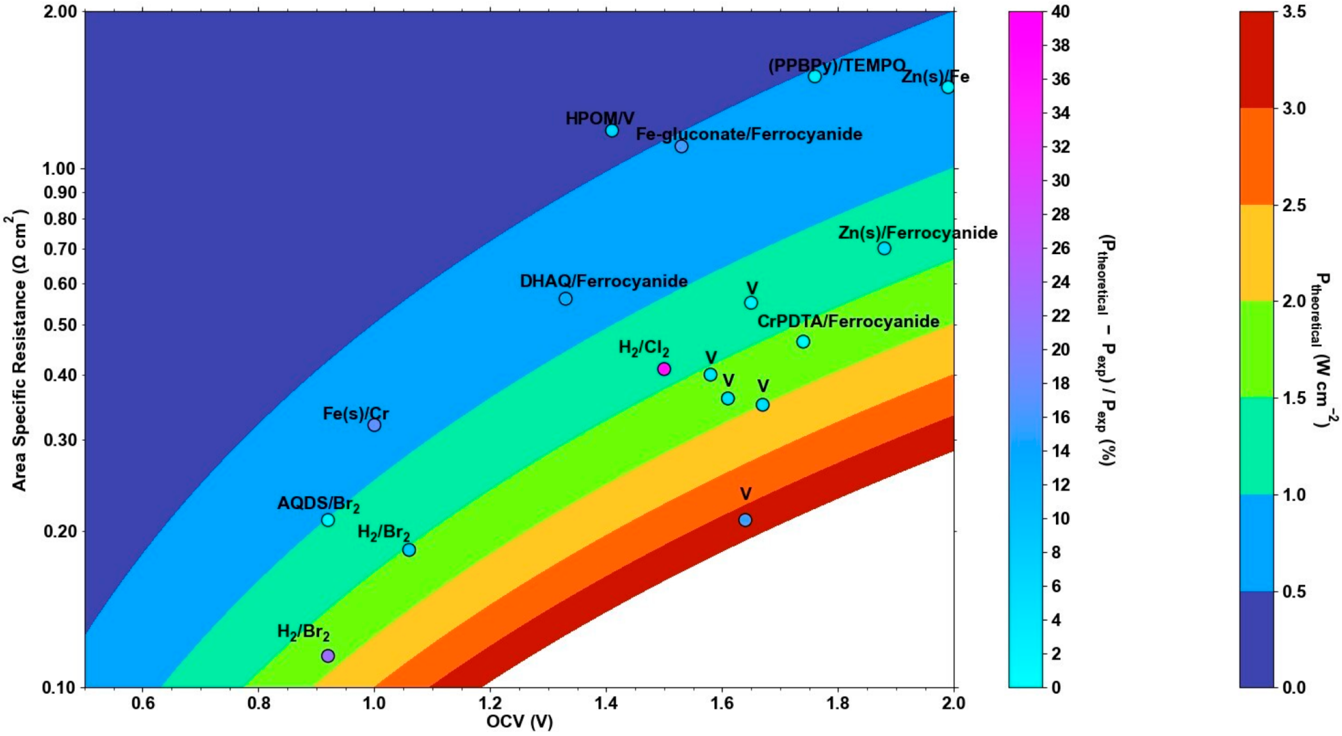

Figure 3. Area-specific resistance versus open-circuit voltage of selected chemistries reported in literature. The first color bar on the right side and the color of the circle next to each chemistry present the error difference between the theoretical and experimental power densities. The contours demonstrate the theoretical power densities calculated from eq 1 for a range of ASRs and OCVs, corresponding to the second color bar on the right.

chemistries reported in the literature. Note that hybrid flow batteries, in which metal deposition occurs during the reaction, are also included. In hybrid flow batteries, the power and energy are not completely independent; nevertheless, they are still sought after for other potential advantages, such as low cost of the involved redox-active species (e.g., zinc). The maximum power data was extracted from polarization curves, the same curves from which the cell OCV and area-specific resistance (ASR) were also obtained. Polarization curves describe the current−voltage relationship of a given battery for a fixed chemical state of charge (SOC). Marker color shows the battery temperature during the experiment yielding the maximum power density, and marker size shows the battery SOC during the same experiment. We include all works, to our knowledge, achieving ≥1 W·cm^{-2} that reported all the relevant experimental data to be included (such as SOC and temperature). We found a total of 11 such works. We also include representative papers for other flow battery chemistries of note that have not achieved 1 W·cm^{-2} to date. Details of each work presented in Figure 1 are found in Table S1. We believe it is informative to break down the data using OCV, distinguishing cells with OCV above the water electrolysis onset voltage (>1.3 V) from those below. We further distinguish in Figure 1 cells which achieved a high power density of >1 W·cm^{-2} from those achieving lower power density. Ultimately, this allows for a breakdown of compiled data into four quadrants: those achieving high power density with a high cell OCV (8 works), those achieving high power density with low OCV (3 works), and those with lower power density with either high OCV or low OCV.

Motivation for our breakdown into the latter quadrants comes from the parameters that affect maximum power density. A simple relationship can be used to approximate the cell's maximum power density, P_{max}:

$$P_{max} = \frac{OCV^2}{4ASR} \quad (1)$$

Here, ASR represents the cell's area-specific resistance (e.g., in units of Ω·cm^2). Equation 1 can be derived (see the Supporting Information (SI)) by assuming a perfectly linear polarization curve, absent of any significant nonlinearities such as those associated with Butler−Volmer-type kinetic losses or mass transport losses (see Figure 2). From eq 1, we can see that ASR and OCV are two important parameters determining P_{max}, and that P_{max} scales as OCV squared. Overall, for a battery to attain high power density >1 W·cm^{-2} with low OCV, the battery chemistry and cell components must be optimized for exceptionally low ASR, for example, <250 mΩ·cm^2 for a cell with 1 V OCV according to eq 1. For cells with higher OCV, larger cell ASRs are allowed, for example, <550 mΩ·cm^2 for a cell with 1.5 V OCV to achieve >1 W·cm^{-2}.

Polarization curves taken at higher SOCs generally yield improved P_{max}, as they are associated with higher OCVs. Thus, measurements of P_{max} shown in Figure 1 are most typically done at SOCs nearing 100%. Although increasing battery temperature can slightly reduce cell OCV, it also allows for significant enhancements in the electrolyte's ionic conductivity, so that higher power can generally be attained by increasing the cell temperature. For linear polarization curves, the maximum power, P_{max}, for a given SOC occurs at a discharge voltage of OCV/2 for a linear polarization curve. Thus, operating the cell at P_{max} is typically not done in practice, as it is associated with low voltage efficiency. However, P_{max} is still a useful metric to compare lab-scale cells and can be used to determine power

https://doi.org/10.1021/acsenergylett.3c01043
ACS Energy Lett. 2023, 8, 3526−3535

density at more realistic operating conditions. For example, the power density when operating at a discharge voltage that is 90% of the cell's OCV is $(9/25)P_{\text{max}}$, assuming a linear polarization curve (see the Supporting Information (SI)).

To get a better sense of the accuracy of eq 1 in predicting real-life P_{max}, we plot in Figure 3 the theoretically calculated P_{max} for various chemistries. The maximum power is plotted versus the cell OCV and ASR extracted from the experimental polarization curve. ASR is extracted from the linear region of the polarization curve (see Table S1), where some experimental curves were approximately linear for all current densities and others showed characteristic nonlinear regions at low or high current densities, which were not used in the ASR calculation. As can be seen, the extracted ASRs vary widely, from 118 mΩ·cm^2 for hydrogen−bromine chemistry to >1300 mΩ·cm^2 for PPBy/TEMPO. Marker color in Figure 3 quantifies the error between the theoretically calculated and experimentally measured P_{max}. For 65% of the chemistries shown here, eq 1 is an accurate predictor of P_{max} given cell OCV and ASR with an error less than 10%. For others, significant error is incurred: up to ∼40%, for example, seen for a hydrogen−chloride system. The presence of significant error is typically correlated with a distinctly nonlinear activation region at low current densities, which reduce measured P_{max} compared to that predicted from eq 1.

2. HIGH-POWER BATTERIES WITH LOW OCV (<1.3 V)

For batteries with lower OCV, achieving high power density relies on reducing the cell's ASR, which can be achieved by combining highly conductive electrolytes and reactants with rapid redox kinetics with engineering optimizations of crucial cell components. This is perhaps best exemplified by hydrogen−bromine redox flow batteries. Hydrobromic acid can achieve an exceptionally high ionic conductivity in excess of 700 mS/cm, so that in cell architectures with thin or highly conductive membranes, >1 W·cm^{-2} is achievable despite a low OCV of ∼1 V (Figure 1).[15,16]

> For batteries with lower open-circuit voltage, achieving high power density relies on reducing the cell's area-specific resistance, which can be achieved by combining highly conductive electrolytes and reactants with rapid redox kinetics with engineering optimizations of crucial cell components.

Interestingly, very few works have demonstrated ASR < 250 mΩ·cm^2 for batteries with OCV < 1.3 V, demonstrating that such degrees of optimization pose a significant challenge. We find three such works, all with bromine-based chemistries such as hydrogen−bromine and quinone−bromine (Figure 2).[15,16,21] Cho et al. achieved $P_{\text{max}} = 1.46$ W·cm^{-2} when operating at room temperature, largely via the use of an ultrathin (15 μm thin) ion-exchange membrane to reduce the cell's ASR.[16] The ASR of their highest power density cell was 184 mΩ·cm^2 (Table S1), with a high-frequency ASR of ∼100 mΩ·cm^2, that is possibly largely attributed to the membrane itself. Livshits et al. achieved 1.5 W·cm^{-2} when operating at 80 °C, through implementation of a thin and highly conductive nanoporous ceramic membrane, leading to a cell ASR of 115 mΩ·cm^2 (Table S1).[15] Chen et al. achieved 1 W·cm^{-2} in an AQDS-bromine battery at 40 °C by reducing cell ASR to 248 mΩ·cm^{-2}.[21] In a separate work, the latter authors provided a detailed dissection of resistances in their cell when operating at room temperature, showing that the DC contributions of the negative and positive electrodes to the cell ASR were, respectively, 143 mΩ·cm^2 and 107 mΩ·cm^2, and the Nafion 212 membrane used contributed 62.1 mΩ·cm^2.[29]

The latter resistance breakdown highlights that, for extremely optimized cells with cell ASR < 250 mΩ·cm^2, the dominant contributor to ASR appears to be the porous electrodes.[29] This was also seen in optimistic calculations of cell and electrode ASR by Milshtein et al., showing the porous electrodes dominated cell resistance by contributing ∼150 mΩ·cm^2 each.[30] This was further confirmed by Alfisi et al. via a detailed resistance breakdown in a membraneless hydrogen−bromine cell, where it was found that the porous positive (bromine) electrode contributed ∼60% of the total cell ASR.[31] The latter work also found only a small contribution (<10%) of the negative (hydrogen) electrode to cell ASR. This suggests that, for electrodes with gas-phase reactants, where fast electrochemical reactions occur at nearly planar interfaces decorated with catalyst nanoparticles, the contribution to cell ASR may be relatively small.[32] This is in contrast to liquid-filled 3D porous electrodes, where even with kinetically fast electrochemical reactions, ion transport through relatively long pores and the presence of distributed reaction zones can couple to dominate cell ASR.[29−31] Following this line of thought, it may be easier to reach <250 mΩ·cm^2 for batteries with only one liquid-solvated reactant, which is thus far borne out by the data in Figure 1. In the figure, we observe that the optimized hydrogen−bromine battery has achieved ∼46% higher power density than the optimized AQDS−bromine cell,[16,21] despite operating at lower temperature (room temperature vs 40 °C). Thus, breakthrough work for achieving yet higher power density may rest on reducing porous electrode ASR via either improved ion transport or catalytic capability. Both Chen et al. and Alfisi et al. identified that the largest contribution to losses in a porous bromine electrode were Faradaic losses due to electron transport across the solid−liquid interface, accounting for ∼50% of the electrode's ASR in both works.[29,31] Thus, one promising strategy is to improve the catalytic capability of the porous electrode via, for example, doping or surface chemistry modifications.

To help guide efforts to further reduce the ASR associated with porous electrodes, it is important to recognize that operation at regimes of extremely low ASR (<250 mΩ·cm^2) leads to different considerations for battery characterization. For example, at such ASR values, transport of electrons through the porous electrode can no longer be neglected in linear circuit models.[29,31] In classical implementations of the transmission line circuit model representing porous electrodes,[33,34] the resistance of the solid phase was justifiably neglected, as it was generally over an order of magnitude smaller than that associated with the electrolyte phase. As batteries push into regimes of extremely high power density, this assumption may no longer be valid. For example, let us consider a typical porous electrode for high-power-density batteries, which has a porosity of $\varepsilon = 80\%$ and a solid-phase (amorphous carbon) conductivity of about 1×10^3 S/m. Implementing a Bruggeman relation for tortuosity, $\tau = \varepsilon^{-0.5}$,[31] the expected ASR of the electrode's solid phase for an electrode 0.5 mm thick would be ∼60 mΩ·cm^2, about that seen in experiments,[35] and significant relative to an optimized cell's ASR of 250 mΩ·cm^2. For these latter cases, the

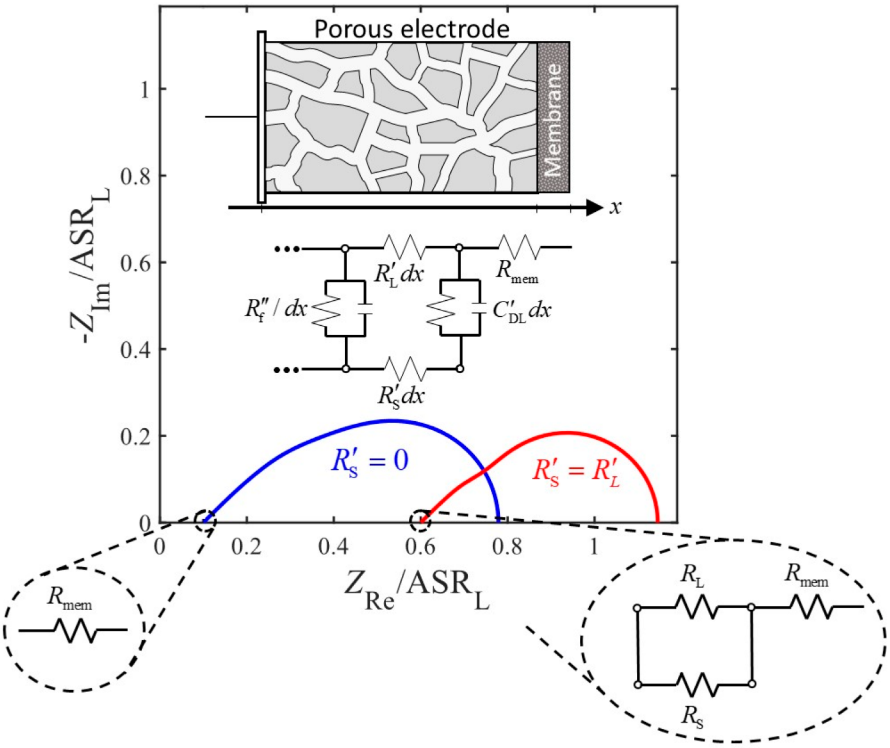

Figure 4. Nyquist plot of the impedance of a porous electrode and membrane in a redox flow battery. The top inset shows a schematic of the physical structure considered, and immediately below is shown the equivalent transmission line circuit model used. Plotted are the impedance curves when the electrode is characterized by negligible solid-phase resistance ($R_s' = 0$, blue curve) and significant solid-phase resistance ($R_s' = R_L'$, red curve). Lower insets show the high-frequency intercept equivalent circuit for the case of negligible and significant solid-phase resistance. Analytical expressions used to plot porous electrode impedance are provided in Alfisi et al.,[31] and parameters used include R_{mem} = 18 mΩ·cm², R_L' = 2600 mΩ·cm², R_F'' = 6.6 mΩ·cm³, and C_{DL}' = 9000 F/cm, as well as the ASR of the electrode's liquid phase, ASR_L = 180 mΩ·cm². Contact resistances, such as those between the electrode and current collector, were neglected.

correct equivalent circuit model must contain the solid-phase resistance, as provided in Figure 4.

> In classical implementations of the transmission line circuit model representing porous electrodes, the resistance of the solid phase was justifiably neglected, as it was generally over an order of magnitude smaller than that associated with the electrolyte phase. As batteries push into regimes of extremely high power density, this assumption may no longer be valid.

Using the correct circuit model with solid-phase resistance leads to important differences in interpreting experimental data. For example, the commonly measured high-frequency intercept of the impedance of the porous electrode or battery is generally interpreted as representing the equivalent resistance of all battery components other than the electrodes, typically dominated by the membrane resistance, R_{mem} (see inset associated with the blue curve in Figure 4). However, for batteries with extremely low ASR, at the high-frequency limit, the equivalent circuit contains also a parallel combination of the liquid and solid-phase resistances of the electrodes, R_L and R_S, respectively (see inset associated with the red curve in Figure 4).[31] Thus, utilization of the classical equivalent circuit to interpret high-power-density battery impedance can lead to errors for *in situ* measurements of the membrane resistance. Using the correct circuit model provides an additional tool to probe electrode quantities, namely the effective *in situ* resistances of the solid and electrolyte phases of the electrode.

At the moment, only cells with both acid-based chemistry and bromine-based posolytes have achieved >1 W·cm^{-2} with a low OCV of <1.3 V (Figure 1). Can a cell with non-acid chemistry and low OCV also reach such lofty levels of power density in the future? For such cells, ion transport through the membrane will typically be associated with higher resistive losses than those achievable with acid chemistry. The molecular diffusivity of the hydronium ion is about twice that of the hydroxide ion, which typically carries membrane current in alkaline chemistry, and is nearly an order of magnitude greater than that of inorganic salt ions, which often carry current in neutral-pH chemistries. Thus, for example, for a typical Nafion 212 membrane (50 μm thickness), a reported membrane ASR for transport of K^+ is 2700 mΩ·cm²,[36] compared to ∼60 mΩ·cm² for the same membrane transporting hydronium ions.[29] However, new membrane chemistries have enabled significant reductions in membrane ASR, as low as 170 mΩ·cm² for K^+ transport.[37] Losses due to ionic transport in porous electrodes may also be an important factor in non-acid chemistries, and detailed breakdowns of resistive losses for such cells would help precisely diagnose such bottlenecks. Overall, neutral-pH chemistries will have a significantly harder challenge achieving <250 mΩ·cm² with low OCV, relative to acid-based chemistries, or even alkaline-based.

3. HIGH-POWER BATTERIES WITH HIGH OCV

The next category of redox flow batteries is based on systems with large open-circuit voltage values (OCV > 1.3 V) that have been reported to deliver high power densities ($P_{\max} > 1.0$ W·cm^{-2}). Possessing large open-circuit voltages brings the advantage of not requiring a significant reduction in the ASR of the battery for achieving high power densities. In order to deliver a power density of 1 W·cm^{-2}, a battery with an OCV between 1.3 and 1.5 V requires an ASR range of 422−563 mΩ·cm^{2}, whereas the ASR must be reduced by about half (250 mΩ·cm^{2}) for a 1.0 V battery to be capable of delivering 1 W·cm^{-2} (see Figure 1). Although large OCV values loosen ASR requirements, systems constructed from redox pairs with either largely negative or largely positive electrochemical potentials (or a combination of both) in an aqueous environment might struggle with the presence of hydrogen evolution or oxygen evolution side reactions or material instability. Side reactions reduce the Coulombic efficiency of the battery and necessitate a recovery strategy such as the use of electrolyte rebalancing. Additionally, material selection can become challenging when dealing with highly oxidative or reductive cell environments. An example is the highly oxidative cerium redox-active species which possess large positive cell potentials of 1.477−1.917 V vs SHE (depending on the supporting electrolyte) but can easily oxidize carbon-based electrodes and anion-exchange membranes.[38,39] Hence, in this regime, an additional effort would be needed for enhancing the electrolyte and cell component stability in the highly reducing and/or oxidative environments of large-OCV aqueous batteries.

As shown in Figures 1 and 3, limited types of batteries fall in the high-power and high-OCV region, and the majority of the data points in this region are based on vanadium chemistry. The all-vanadium flow battery (VRFB) possesses an OCV of ∼1.4 V at 50% SOC.[40] Although thermodynamically the electrochemical potential of V^{2+}/V^{3+} on the negative side of VRFB systems lies slightly out of the water stability window ($E^{\circ}_{V^{2+}/V^{3+}} \approx -0.255$ V versus SHE), kinetically the hydrogen evolution side reaction is too slow at such overpotentials. Hence, with proper distribution of local currents and prevention of large local overpotentials, the presence of side reactions in VRFBs is negligible. Nevertheless, in the event of gas evolution and cell imbalance, strategies such as external cell rebalancing[41] can be employed.

The VRFBs reported in the high-power, high-OCV regime have all achieved power densities between 1.2 and 1.9 W·cm^{-2} with area-specific resistances of 400−500 mΩ·cm^{2},[12−14,26] with the exception of the work by Jiang et al. In the latter, a power density of 2.78 W·cm^{-2} was achieved by reducing the system's ASR to 223 mΩ·cm^{2}.[9] The work of Jiang et al. is, to our knowledge, the sole example of a cell with both high OCV and exceptionally low ASR (<250 mΩ·cm^{2}) and will be further discussed in the next section. The rest of the reported power densities in this regime are discussed in the present section. These high power densities were achieved by utilizing highly conductive, low-resistance membranes[12] capable of reducing the ohmic resistance of the cell, or by use of catalysts for reducing vanadium redox kinetic losses,[26] or by fabrication of high-surface-area porous electrodes capable of cutting the electrode kinetic and mass-transfer losses in the system.[13,14]

A prominent non-vanadium system in this category is a neutral pH flow battery based on a CrPDTA metal complex paired with ferrocyanide.[8] CrPDTA has an electrochemical potential of −1.1 V vs SHE and thus is 570 mV more negative than the hydrogen evolution reaction (HER) potential at pH 9. Nevertheless, the HER seems to have occurred negligibly in the presence of CrPDTA. This extension of the kinetic water stability window is hypothesized to occur due to the inhibition of water coordination to the Cr metal center, creating a large kinetic barrier for HER.[42] The CRPDTA/ferrocyanide system possesses a large OCV of 1.62 V, and thus, as the contour plots of power density in Figure 3 show, a 1 W·cm^{-2} cell can be easily achieved by reducing the ASR to 656 mΩ·cm^{2}. Benefiting from such a large cell voltage, Robb et al.[8] focused on reducing the ASR of the cell by optimizing the membrane. Note that the CRPDTA/ferrocyanide system is operated at a neutral pH with potassium ions as charge carriers through the membrane as opposed to protons in acid-based flow batteries such as all-vanadium. The ASR of a flow battery assembled with Nafion 212 in 1 M KCl is reported to be 2.7 Ω·cm^{2}, whereas this number is only 0.2 Ω·cm^{2} for a cell assembled with Nafion 212 in 1 M HCl,[36] clearly demonstrating the lower conductivity of potassium ions through Nafion 212 compared to protons. By using an alternative membrane (E-610 K), which is thinner and has a higher conductivity for potassium ions (ASR = 0.3 Ω·cm^{2} in a cell with 1 M KCl), and by utilizing a bismuth catalyst and a higher operating temperature (40 °C), the CRPDTA/ferrocyanide RFB achieved a high power density of 1.63 W·cm^{-2}.[8]

The zinc redox couple is another promising redox-active species for hybrid flow batteries, with a large negative electrochemical potential of −1.245 V vs SHE in alkaline conditions.[27] A large cell voltage of ∼1.8 V at 50% SOC is achieved when $Zn(OH)_4^{2-}/Zn$ is paired with an $Fe(CN)_6^{3-}/Fe(CN)_6^{4-}$ redox couple, presenting a great opportunity for constructing a high-power hybrid flow battery. The zinc/ferrocyanide battery cycling is, however, complicated by the formation of dendrites during zinc deposition, which can break the membrane and result in a short-circuit. Yuan et al.[27] resolved dendrite formation by using an alternative negatively charge nanoporous membrane. The dendrite formation was successfully inhibited by the repulsion between the negatively charged membrane and the zincate ions. This battery demonstrated a maximum power density of 1.056 W·cm^{-2} at 50% SOC and 1.2 W·cm^{-2} at 100% SOC. Given the large cell voltage of the cell, along with the abundance and the low cost of zinc and iron metals, further investigation into other approaches for ASR reduction of zinc/ferrocyanide batteries for achieving a high-power flow battery would be attractive.

> This investigation reveals three distinct strategies for achieving high open-circuit voltage: kinetic inhibition, dual-membrane architecture, or construction of the cell with non-aqueous chemistries.

More broadly, investigating the high-voltage quadrants in Figure 1 reveals three distinct strategies for achieving high OCV: kinetic inhibition, dual-membrane architecture, or construction of the cell with non-aqueous chemistries. The first strategy, kinetic inhibition, as shown for the cases of vanadium and CrPDTA, involves developing redox couples with OCV > 1.3 V, but together with electrodes or redox-active elements that simultaneously inhibit water splitting. This strategy has yielded several devices achieving >1 W·cm^{-2} (Figure 1).[43] The second strategy is use of a dual-membrane cell architecture, which enables the pairing of redox-active species with positive and negative ionic charges and at different pH values—pairings not possible through conventional single-membrane cell configurations. For example, the Zn/Fe cell, which couples an acidic Fe posolyte and an alkaline Zn negolyte, results in a high OCV of ∼2.0 V and a power density of ∼0.676 W·cm^{-2} (Figure 1), the highest, to our knowledge, to date with dual-membrane architecture.[23] This strategy necessarily increases the cell ASR by addition of a second membrane and a third electrolyte channel, but future optimizations of such cells may allow for breakthrough >1 W·cm^{-2} power densities. For example, in the latter Zn/Fe system, an ASR of 2.3 Ω·cm^2 was reported.[23] A quick calculation of the middle channel ASR (thickness, L = 0.5 mm, divided by electrolyte conductivity, ε = 0.17 S cm^{-1}) results in an ASR contribution of only ∼0.3 Ω·cm^2, and thus likely the cell ASR was dominated by membrane contributions. Note that it is important to assess the financial implications of utilizing an extra membrane, as it could potentially counteract the cost-saving benefits derived from achieving a high power density and reducing stack size. The third strategy involves the AzoB/DBMMB flow battery,[11] which here represents one of the highest power densities achieved by non-aqueous cells. Non-aqueous flow batteries can provide up to 4.5 V without solvent decomposition,[44] but reducing the ASR is more challenging due to the relatively low electrolyte conductivity. The AzoB/DBMMB cell demonstrated 2.5 V OCV and a maximum power density of 0.336 W·cm^{-2}, but with a cell ASR of ∼4 Ω·cm^2. The ASR must be reduced by at least 40% to achieve ≥1 W·cm^{-2} power density, motivating further research into increasing the ionic conductivity of non-aqueous redox species.

4. COMBINING HIGH OCV AND LOW ASR FOR ULTRAHIGH POWER DENSITY

The strategies of reducing cell ASR or increasing OCV can be combined, leading to ultrahigh power density. In theory, one can achieve >2.5 W·cm^{-2} at room temperature, for example for a battery with an ASR of 250 mΩ·cm^2 and 1.6 V OCV which follows eq 1. From Figure 1, the chemistry to-date which best combines these two approaches has employed vanadium. Prominently, Jiang et al. demonstrated up to 2.78 W·cm^{-2} with all-vanadium chemistry by leveraging a high OCV of 1.64 V and electrode and membrane optimizations to attain a cell ASR of 223 mΩ·cm^2.[9] This means that likely each porous electrode had an ASR $\lesssim$ 100 mΩ·cm^2, as it is reasonable to attribute $\gtrsim$20 mΩ·cm^2 to the Nafion 211 membrane for the 3 M H_2SO_4 electrolyte used. Looking more deeply into these exceptional results, as the only flow battery to our knowledge to achieve >2 W·cm^{-2}, involves an analysis into the exceptionally low porous electrode ASR obtained. In previous detailed resistance breakdowns for batteries using hydrogen−bromine and bromine−quinone chemistry,[29,31] as well as optimistic calculations for electrode ASR,[30] the porous positive electrodes showed an ASR > 100 mΩ·cm^2. Further, the bromine redox couple is generally characterized by faster kinetics than vanadium, and indeed the polarization curve presented by Jiang et al. showed a characteristic nonlinear activation region at low currents, indicative of substantial Faradaic losses—features not seen in the linear curves associated with bromine-based batteries.[29,31] Also, there is about equal electrolyte ionic conductivity between that used in vanadium batteries and bromine batteries, with ∼700 mS/cm for 3 M HBr and 3 M H_2SO_4 at room temperature, and seemingly negligible mass transport losses for all batteries considered here due to operation at high electrolyte flow rates and high SOC. Therefore, gaining a comprehensive understanding of the underlying factors that enabled the attainment of such a remarkable power density in the work of Jiang et al. is crucial. In our opinion, detailed *ex situ* characterization of such porous electrodes is warranted to provide strong explanations for the exceptional performance attained, for example including breakdowns of solid-phase, liquid-phase, and Faradaic contributions to total electrode ASR. Such investigations would not only deepen our understanding of high-power-density systems but also provide valuable guidance for reducing electrode ASR in future designs.

5. MASS TRANSFER FOR HIGH-POWER-DENSITY BATTERIES

At current densities approaching the limiting current density of the battery, mass-transfer losses can become significant. Such mass transport losses can lower the discharge voltage, invalidating eq 1 and potentially lowering $P_{\max}$, as well as inhibiting high power density over a reasonable SOC range (e.g., 20%−80% SOC). The limiting current density ($i_{\lim}$) of a cell, for the case where one of the reactants is limiting, can be written as follows:

$$i_{\lim} = nFk_{\mathrm{m}}C_{\mathrm{bulk}} \tag{2}$$

where n is the number of electrons transferred, F is the Faraday constant, C_{bulk} is the bulk concentration of the reactant, and k_{m} is the velocity-dependent mass-transfer coefficient, which is affected by the electrode pore structure and the flow field design. For infinitely fast reactant diffusion, $k_{\mathrm{m}} = v$, where v is the average velocity of the reactant entering the flow field. For a linear polarization curve, eq 1 is accurate as long as, at the extremes of the target SOC window, $i_{\lim} > i_{P_{\max}}$, where $i_{P_{\max}}$ is the current density at the SOC-dependent maximum power. If we assume operating at V = 0.9OCV, then the needed operating current would be $0.1\frac{\mathrm{OCV}}{\mathrm{ASR}}$, and the output power would be $(9/25)P_{\max}$. Consequently, we need to have, for the entire target SOC window,

$$k_{\mathrm{m}}C_{\mathrm{bulk}} > 0.1\frac{\mathrm{OCV}}{nF\,\mathrm{ASR}} \tag{3}$$

for the power of $(9/25)P_{\max}$ to be provided without complications from the mass-transfer limitation. This result highlights that $i_{\lim}$ can be increased by employing higher C_{bulk}, with an upper limit based on the electroactive species' solubility. Bulk concentration is also dependent on the SOC of the battery, and thus mass-transfer limitations become more pronounced toward the end of the charge and discharge phases, at the extremes of the SOC window. Limiting current can also be enhanced by employing higher flow velocity or engineering pore structure for improved k_{m}. Increasing the operating flow rate requires consuming a larger pump power, and for high-power-density cells that can attain high-current-density operation, pump power loss should be considered when calculating the system's net power, $P_{\mathrm{net}} = P_{\mathrm{cell}} - P_{\mathrm{pump}}$. The pump power required (for 2 pumps) can be calculated from $P_{\mathrm{pump}} = \sum_{i=\mathrm{pos,neg}} Q_i \Delta p_i/\eta_{\mathrm{pump}}$, where η_{pump} is the pump efficiency, Q_i is the flow rate, and Δp_i is the flow system pressure loss at the positive (i = pos) or negative (i = neg) side of the cell. The pressure loss is caused by the stack and the flow tubing (see SI section 3). For example, for an all-vanadium redox flow battery at 50% SOC (1 M vanadium at each oxidations state), OCV = 1.4 V, and ASR = 0.49 Ω·cm^2 (P_{max} = 1 W·cm^{-2}, P = 0.36 W·cm^{-2} at V_p = 0.9OCV), the mass-transfer coefficient has to be at least 0.003 cm s^{-1} to satisfy eq 3. Using an empirical equation derived for carbon fiber/felt electrodes,[45] relating the mass-transfer coefficient to velocity ($k_m = 1.6 \times 10^{-4} v^{0.4}$ in SI units), we can approximately find that a velocity of 1.47 cm s^{-1} is needed. From this velocity, a pressure loss of 9.78×10^3 N m^{-2} would be expected in the stack (ignoring pressure losses in the pipe), which would result in a pump power of 0.034 W·cm $^{-2}$, constituting 9% of the cell's power output. Nevertheless, doing these calculations in reverse reveals that, for such an electrode, the pump power would become equal to the cell's power output (zero net power) when the SOC drops to 30% during discharge. Consequently, in the context of high-power-density cells, the contribution of the pump power, especially at the extremes of the target SOC window, must be taken into account.

> In the context of high-power-density cells, the contribution of the pump power, especially at the extremes of the target state-of-charge window, must be taken into account.

To reduce the need for operating at high flow rates and consequently having large pump losses, flow field and pore structure engineering for improved k_m (eq 2) can be implemented. Several studies have investigated the performance of the common flow field designs (parallel, serpentine, and interdigitated) as well as newer and niche designs (e.g., spiral) in redox flow batteries.[46−49] For example, serpentine flow fields, with their single path extending over the electrode surface, provide lower pressure drops compared to the interdigitated flow fields with dead-end channels. Nevertheless, the mass-transfer rates are higher with interdigitated design due to the forced convective flow induced from the dead-end paths. This illustrates the importance of the choice of flow field design and its impact on pressure drop and the net power output of the battery. As for the electrode structure, electrodes with bimodal pore distribution[50] have shown improved mass transfer, which is attributed to simultaneous enhancements in permeability and surface area in the electrode. While such performance observations are beneficial, elucidation of the fundamental relationship between the electrode microstructure and the overall performance of the battery would allow for informed design of electrode structures. Exploring microstructure−performance relationships has been the theme of several studies on commercial carbon paper and cloth electrodes.[51−53] Such studies have reflected the complex local flow behavior within different porous commercial electrode structures; however, drawing broad generalizations about the effects of microstructure on the performance is still challenging. Tools such as *in situ* visualization techniques via fluorescence microscopy coupled with electrochemistry can aid in developing a fundamental understanding.[54] This fundamental understanding can be deepened with computational modeling and predictive tools to accelerate the design of porous electrodes with the best combination of properties for high-power redox flow batteries.[55]

6. SUMMARY

Given that widespread commercialization of RFBs is contingent on cost reduction to meet the target installation price of $100/kWh, major efforts should be directed toward not only developing low-cost electrolytes but also enhancing power density in order to cut stack costs. To date, a limited number of studies have reported peak output power densities above 1 W·cm^{-2} (Figure 1), and the majority of such works have studied vanadium RFBs. The highest power density ever reported for RFBs is 2.78 W·cm^{-2} for a VRFB system at room temperature. We argue that, for systems claiming exceptionally high power density, such claims should be combined with detailed dissection of voltage losses to impart insight into the source of this exceptional behavior and strengthen such claims. High cell OCV is advantageous for reaching high power density, but high ASR has, in many cases, kept the peak power density below 1 W·cm^{-2}. To reach high power densities for cells with OCV below the thermodynamic water stability window (<1.3 V), minimization of cell ASR is crucial. Cell characterization in this latter regime must be done with care—for example, including the effect of porous electrode solid-phase resistance in equivalent circuit models. Developing insight into the enabling characteristics of high-power-density RFBs by conducting careful system characterization and applying such insight into other RFBs can pave the way for maximizing the power density of RFBs and thereby accelerating their widespread deployment.

■ ASSOCIATED CONTENT

Supporting Information

The Supporting Information is available free of charge at https://pubs.acs.org/doi/10.1021/acsenergylett.3c01043.

Table S1, derivations of power equations, and step-by-step calculation of the pump power loss (PDF)

■ AUTHOR INFORMATION

Corresponding Authors

Matthew E. Suss − *Faculty of Mechanical Engineering, Technion−Israel Institute of Technology, Haifa 3200003, Israel;* orcid.org/0000-0002-3813-2274;
Email: mesuss@me.technion.ac.il
Michael J. Aziz − *John A. Paulson School of Engineering and Applied Sciences, Harvard University, Cambridge, Massachusetts 02138, United States;* orcid.org/0000-0001-9657-9456; Email: maziz@harvard.edu

Authors

Kiana Amini − *John A. Paulson School of Engineering and Applied Sciences, Harvard University, Cambridge, Massachusetts 02138, United States*
Amit N. Shocron − *Faculty of Mechanical Engineering, Technion−Israel Institute of Technology, Haifa 3200003, Israel;* orcid.org/0000-0002-9247-905X

Complete contact information is available at:
https://pubs.acs.org/10.1021/acsenergylett.3c01043

Notes

The authors declare no competing financial interest.

Biographies

Kiana Amini is a Postdoctoral Fellow at Harvard University. She has an extensive background in the development of redox flow batteries for energy storage applications. Starting Fall 2023, she will be an Assistant

Professor in the Department of Materials Engineering at the University of British Columbia.

Amit N. Shocron is a Ph.D. candidate at Technion under the supervision of Prof. Matthew E. Suss. He received his B.S. and M.S. in Mechanical Engineering also at Technion. His research focuses on theoretical modeling of electrochemical systems at the water-energy nexus.

Matthew E. Suss earned a Ph.D. from Stanford in 2013. He was a Lawrence Scholar at Lawrence Livermore National Lab (2010−2013) and a Postdoctoral Associate at MIT (2013−2014). Now an Associate Professor at Technion, he leads the Energy & Environmental Innovations Lab and is an Associate Editor at RSC. https://meeng.technion.ac.il/members/matthew-suss/

Michael J. Aziz is Professor of Materials and Energy Technologies at the Harvard School of Engineering and Applied Sciences. He is co-recipient of the 2019 Energy Frontiers Prize from Eni for the invention and development of the aqueous organic flow battery. He has a significant financial stake in Quino Energy, Inc. https://aziz.seas.harvard.edu/

■ ACKNOWLEDGMENTS

This research was supported by the National Science Foundation through grant CBET-1914543 and by U.S. DOE award DE-AC05-76RL01830 through PNNL subcontract 654799. K.A. was supported in part by U.S. DOE award DE-AC05-76RL01830 through PNNL subcontract 654799 and in part through the Natural Sciences and Engineering Research Council of Canada (NSERC) Postdoctoral Fellowship (PDF) program [application number PDF - 557232-2021].

■ REFERENCES

(1) Renewables 2022: Analysis and Forecasts to 2026. International Energy Agency (IEA), December 2022. https://www.iea.org/reports/renewables-2022

(2) Office of Energy Projects Energy Infrastructure Update, June 2022. https://cms.ferc.gov/media/energy-infrastructure-update-june-2022 (accessed March 2023).

(3) Office of Energy Projects Energy Infrastructure Update, December 2019. https://www.caba.org/wp-content/uploads/2020/06/IS-2020-65.pdf (accessed April 2023).

(4) Ferreira, H. L.; Garde, R.; Fulli, G.; Kling, W.; Lopes, J. P. Characterisation of electrical energy storage technologies. *Energy* **2013**, *53*, 288−298.

(5) Viswanathan, V.; Mongird, K.; Franks, R.; Li, X.; Sprenkle, V. *2022 Grid Energy Storage Technology Cost and Performance Assessment*, Technical Report Publication No. PNNL-33283; Pacific Northwest National Laboratory, August 2022.

(6) Salles, M. B. C.; Gadotti, T. N.; Aziz, M. J.; Hogan, W. W. Potential revenue and breakeven of energy storage systems in PJM energy markets. *Environ. Sci. Pollut Res. Int.* **2021**, *28* (10), 12357−12368.

(7) Minke, C.; Turek, T. Materials, system designs and modelling approaches in techno-economic assessment of all-vanadium redox flow batteries - A review. *J. Power Sources* **2018**, *376*, 66−81.

(8) Robb, B. H.; Waters, S. E.; Saraidaridis, J. D.; Marshak, M. P. Realized potential as neutral pH flow batteries achieve high power densities. *Cell Rep. Phys. Sci.* **2022**, *3* (11), 101118.

(9) Jiang, H. R.; Sun, J.; Wei, L.; Wu, M. C.; Shyy, W.; Zhao, T. S. A high power density and long cycle life vanadium redox flow battery. *Energy Storage Mater.* **2020**, *24*, 529−540.

(10) Lin, K.; Chen, Q.; Gerhardt, M. R.; Tong, L.; Kim, S. B.; Eisenach, L.; Valle, A. W.; Hardee, D.; Gordon, R. G.; Aziz, M. J.; Marshak, M. P. Alkaline quinone flow battery. *Science* **2015**, *349* (6255), 1529−1532.

(11) Xu, D.; Zhang, C.; Zhen, Y.; Zhao, Y.; Li, Y. A high-rate nonaqueous organic redox flow battery. *J. Power Sources* **2021**, *495*, 229819.

(12) Pezeshki, A. M.; Tang, Z. J.; Fujimoto, C.; Sun, C. N.; Mench, M. M.; Zawodzinski, T. A. Full Cell Study of Diels Alder Poly(phenylene) Anion and Cation Exchange Membranes in Vanadium Redox Flow Batteries. *J. Electrochem. Soc.* **2016**, *163* (1), A5154−A5162.

(13) Sun, J.; Jiang, H. R.; Wu, M. C.; Fan, X. Z.; Chao, C. Y. H.; Zhao, T. S. Aligned hierarchical electrodes for high-performance aqueous redox flow battery. *Appl. Energy* **2020**, *271*, 115235.

(14) Sun, J.; Wu, M. C.; Fan, X. Z.; Wan, Y. H.; Chao, C. Y. H.; Zhao, T. S. Aligned microfibers interweaved with highly porous carbon nanofibers: A Novel electrode for high-power vanadium redox flow batteries. *Energy Storage Mater.* **2021**, *43*, 30−41.

(15) Livshits, V.; Ulus, A.; Peled, E. High-power H_2/Br_2 fuel cell. *Electrochem. Commun.* **2006**, *8* (8), 1358−1362.

(16) Cho, K. T.; Albertus, P.; Battaglia, V.; Kojic, A.; Srinivasan, V.; Weber, A. Z. Optimization and Analysis of High-Power Hydrogen/Bromine-Flow Batteries for Grid-Scale Energy Storage. *Energy Technol.* **2013**, *1* (10), 596−608.

(17) Gao, M.; Salla, M.; Song, Y.; Wang, Q. High-Power Near-Neutral Aqueous All Organic Redox Flow Battery Enabled with a Pair of Anionic Redox Species. *Angew. Chem., Int. Ed.* **2022**, *61* (41), No. e202208223.

(18) Weng, G.-M.; Li, Z.; Cong, G.; Zhou, Y.; Lu, Y.-C. Unlocking the capacity of iodide for high-energy-density zinc/polyiodide and lithium/polyiodide redox flow batteries. *Energy Environ. Sci.* **2017**, *10* (3), 735−741.

(19) Ai, F.; Wang, Z.; Lai, N.-C.; Zou, Q.; Liang, Z.; Lu, Y.-C. Heteropoly acid negolytes for high-power-density aqueous redox flow batteries at low temperatures. *Nat. Energy* **2022**, *7* (5), 417−426.

(20) Wu, M. C.; Zhao, T. S.; Jiang, H. R.; Zeng, Y. K.; Ren, Y. X. High-performance zinc bromine flow battery via improved design of electrolyte and electrode. *J. Power Sources* **2017**, *355*, 62−68.

(21) Chen, Q.; Gerhardt, M. R.; Hartle, L.; Aziz, M. J. A Quinone-Bromide Flow Battery with 1 $W \cdot cm^{-2}$ Power Density. *J. Electrochem. Soc.* **2016**, *163* (1), A5010−A5013.

(22) Zeng, Y. K.; Zhou, X. L.; Zeng, L.; Yan, X. H.; Zhao, T. S. Performance enhancement of iron-chromium redox flow batteries by employing interdigitated flow fields. *J. Power Sources* **2016**, *327*, 258−264.

(23) Gong, K.; Ma, X.; Conforti, K. M.; Kuttler, K. J.; Grunewald, J. B.; Yeager, K. L.; Bazant, M. Z.; Gu, S.; Yan, Y. A zinc-iron redox-flow battery under $100 per kW h of system capital cost. *Energy Environ. Sci.* **2015**, *8* (10), 2941−2945.

(24) Liu, X.; Li, T.; Yuan, Z.; Li, X. Low-cost all-iron flow battery with high performance towards long-duration energy storage. *J. Energy Chem.* **2022**, *73*, 445−451.

(25) Xia, Y.; Ouyang, M.; Yufit, V.; Tan, R.; Regoutz, A.; Wang, A.; Mao, W.; Chakrabarti, B.; Kavei, A.; Song, Q.; Kucernak, A. R.; Brandon, N. P. A cost-effective alkaline polysulfide-air redox flow battery enabled by a dual-membrane cell architecture. *Nat. Commun.* **2022**, *13* (1), 2388.

(26) Xia, L.; Long, T.; Li, W.; Zhong, F.; Ding, M.; Long, Y.; Xu, Z.; Lei, Y.; Guan, Y.; Yuan, D.; Zhang, Y.; Jia, C.; Sun, L.; Sun, Q. Highly Stable Vanadium Redox-Flow Battery Assisted by Redox-Mediated Catalysis. *Small* **2020**, *16* (38), No. e2003321.

(27) Yuan, Z.; Liu, X.; Xu, W.; Duan, Y.; Zhang, H.; Li, X. Negatively charged nanoporous membrane for a dendrite-free alkaline zinc-based flow battery with long cycle life. *Nat. Commun.* **2018**, *9* (1), 3731.

(28) Huskinson, B.; Rugolo, J.; Mondal, S. K.; Aziz, M. J. A high power density, high efficiency hydrogen-chlorine regenerative fuel cell with a low precious metal content catalyst. *Energy Environ. Sci.* **2012**, *5* (9), 8690.

(29) Chen, Q.; Gerhardt, M. R.; Aziz, M. J. Dissection of the Voltage Losses of an Acidic Quinone Redox Flow Battery. *J. Electrochem. Soc.* **2017**, *164* (6), A1126−A1132.

(30) Milshtein, J. D.; Darling, R. M.; Drake, J.; Perry, M. L.; Brushett, F. R. The Critical Role of Supporting Electrolyte Selection on Flow Battery Cost. *J. Electrochem. Soc.* **2017**, *164* (14), A3883−A3895.

(31) Alfisi, D.; Shocron, A. N.; Gloukhovski, R.; Vermaas, D. A.; Suss, M. E. Resistance Breakdown of a Membraneless Hydrogen-Bromine Redox Flow Battery. *ACS Sustain Chem. Eng.* **2022**, *10* (39), 12985−12992.

(32) Manzi-Orezzoli, V.; Siegwart, M.; Scheuble, D.; Chen, Y.-C.; Schmidt, T. J.; Boillat, P. Impact of the Microporous Layer on Gas Diffusion Layers with Patterned Wettability I: Material Design and Characterization. *J. Electrochem. Soc.* **2020**, *167* (6), 064516.

(33) Newman, J. S.; Tobias, C. W. Theoretical Analysis of Current Distribution in Porous Electrodes. *J. Electrochem. Soc.* **1962**, *109*, 1183.

(34) de Levie, R. On Porous Electrodes in Electrolyte Solutions. *Electrochim. Acta* **1963**, *8*, 751−780.

(35) Tjaden, B.; Cooper, S. J.; Brett, D. J. L.; Kramer, D.; Shearing, P. R. On the origin and application of the Bruggeman correlation for analysing transport phenomena in electrochemical systems. *Curr. Opin. Chem. Eng.* **2016**, *12*, 44−51.

(36) Waters, S. E.; Thurston, J. R.; Armstrong, R. W.; Robb, B. H.; Marshak, M. P.; Reber, D. Holistic design principles for flow batteries: Cation dependent membrane resistance and active species solubility. *J. Power Sources* **2022**, *520*, 230877.

(37) Zuo, P.; Ye, C.; Jiao, Z.; Luo, J.; Fang, J.; Schubert, U. S.; McKeown, N. B.; Liu, T. L.; Yang, Z.; Xu, T. Near-frictionless ion transport within triazine framework membranes. *Nature* **2023**, *617*, 299.

(38) Leung, P. K.; Ponce-de-León, C.; Low, C. T. J.; Shah, A. A.; Walsh, F. C. Characterization of a zinc-cerium flow battery. *J. Power Sources* **2011**, *196* (11), 5174−5185.

(39) Amini, K.; Pritzker, M. D. Life-cycle analysis of zinc-cerium redox flow batteries. *Electrochim. Acta* **2020**, *356*, 136785.

(40) Geiser, J.; Natter, H.; Hempelmann, R.; Morgenstern, B.; Hegetschweiler, K. Photometrical Determination of the State-of-Charge in Vanadium Redox Flow Batteries Part II: In Combination with Open-Circuit-Voltage. *Z. Phys. Chem.* **2019**, *233* (12), 1695−1711.

(41) Corcuera, S.; Skyllas-Kazacos, M. State-of-charge monitoring and electrolyte rebalancing methods for the vanadium redox flow battery. *Eur. Chem. Bull.* **2012**, *1* (12), 511−519.

(42) Robb, B. H.; Waters, S. E.; Marshak, M. P. Evaluating aqueous flow battery electrolytes: a coordinated approach. *Dalton Trans.* **2020**, *49* (45), 16047−16053.

(43) Perry, M. L.; Rodby, K. E.; Brushett, F. R. Untapped Potential: The Need and Opportunity for High-Voltage Aqueous Redox Flow Batteries. *ACS Energy Lett.* **2022**, *7* (2), 659−667.

(44) Darling, R. M.; Gallagher, K. G.; Kowalski, J. A.; Ha, S.; Brushett, F. R. Pathways to low-cost electrochemical energy storage: a comparison of aqueous and nonaqueous flow batteries. *Energy Environ. Sci.* **2014**, *7* (11), 3459−3477.

(45) Schmal, D.; Van Erkel, J.; Van Duin, P. J. Mass transfer at carbon fibre electrodes. *J. Appl. Electrochem.* **1986**, *16*, 422−430.

(46) Dennison, C. R.; Agar, E.; Akuzum, B.; Kumbur, E. C. Enhancing Mass Transport in Redox Flow Batteries by Tailoring Flow Field and Electrode Design. *J. Electrochem. Soc.* **2016**, *163* (1), A5163−A5169.

(47) Kumar, S.; Jayanti, S. Effect of flow field on the performance of an all-vanadium redox flow battery. *J. Power Sources* **2016**, *307*, 782−787.

(48) Zheng, Q.; Xing, F.; Li, X.; Ning, G.; Zhang, H. Flow field design and optimization based on the mass transport polarization regulation in a flow-through type vanadium flow battery. *J. Power Sources* **2016**, *324*, 402−411.

(49) Darling, R. M.; Perry, M. L. The Influence of Electrode and Channel Configurations on Flow Battery Performance. *J. Electrochem. Soc.* **2014**, *161* (9), A1381−A1387.

(50) Zhou, X. L.; Zhao, T. S.; Zeng, Y. K.; An, L.; Wei, L. A highly permeable and enhanced surface area carbon-cloth electrode for vanadium redox flow batteries. *J. Power Sources* **2016**, *329*, 247−254.

(51) Tenny, K. M.; Greco, K. V.; van der Heijden, M.; Pini, T.; Mularczyk, A.; Vasile, A.-P.; Eller, J.; Forner-Cuenca, A.; Chiang, Y.-M.; Brushett, F. R. A Comparative Study of Compressive Effects on the Morphology and Performance of Carbon Paper and Cloth Electrodes in Redox Flow Batteries. *Energy Technol.* **2022**, *10* (8), 2101162.

(52) Tenny, K. M.; Forner-Cuenca, A.; Chiang, Y.-M.; Brushett, F. R. Comparing Physical and Electrochemical Properties of Different Weave Patterns for Carbon Cloth Electrodes in Redox Flow Batteries. *J. Electrochem. Energy Conversion Storage* **2020**, *17* (4), 4046661.

(53) Forner-Cuenca, A.; Penn, E. E.; Oliveira, A. M.; Brushett, F. R. Exploring the Role of Electrode Microstructure on the Performance of Non-Aqueous Redox Flow Batteries. *J. Electrochem. Soc.* **2019**, *166* (10), A2230−A2241.

(54) Wong, A. A.; Rubinstein, S. M.; Aziz, M. J. Direct visualization of electrochemical reactions and heterogeneous transport within porous electrodes in operando by fluorescence microscopy. *Cell Rep. Phys. Sci.* **2021**, *2* (4), 100388.

(55) Roy, T.; Salazar de Troya, M. A.; Worsley, M. A.; Beck, V. A. Topology optimization for the design of porous electrodes. *Struct. Multidisc. Optim.* **2022**, *65* (6), 171.

Supplementary Information

Pathways to High-Power-Density Redox Flow Batteries

Kiana Amini, Amit N. Shocron, Matthew E. Suss*, Michael J. Aziz*

K. Amini, M. J. Aziz, Harvard John A. Paulson School of Engineering and Applied Sciences, 29 Oxford Street, Cambridge, Massachusetts 02138, USA.

A. N. Shocron, M. E. Suss, Faculty of Mechanical Engineering, Technion−Israel Institute of Technology, Haifa3200003, Israel.

*****Co-corresponding Author: mesuss@me.technion.ac.il (Matthew E. Suss), maziz@harvard.edu (Michael J. Aziz).

1) Derivation of the maximum power density in the absence of kinetic and mass transfer losses

In the absence of mass transfer and kinetic losses, the power density of the battery is only affected by ohmic losses (ASR). Thus:

$$P = OCV * i - ASR * i^2 \quad [1]$$

To find the maximum power density (P_{max}), the current at the point of P_{max} is derived from taking a derivative of Eq. [1] with respect to current:

$$\frac{dP}{di} = OCV - 2 * ASR * i = 0 \; [2]$$

$$i_{P_{max}} = \frac{OCV}{2ASR} \quad [3]$$

Substituting Eq. [3] in Eq. [1], we find:

$$P_{max} = \frac{OCV^2}{4 * ASR} \quad [4]$$

2) Derivation of the power density at 90% galvanic voltage efficiency

Assuming a 90% galvanic voltage efficiency, the discharge voltage would be 0.9*OCV. At this discharge voltage the current would be:

$$0.9 * OCV = OCV - ASR * i_{0.9} \quad [5]$$

$$i_{0.9} = 0.1 \frac{OCV}{ASR} \qquad [6]$$

Substituting Eq. [6] into Eq. [1] would yield:

$$P_{0.9} = OCV * i_{0.9} - ASR * i_{0.9}^2 \quad [7]$$

$$P_{0.9} = \left(\frac{9}{25}\right) * \frac{OCV^2}{4 * ASR} \quad [8]$$

3) Calculation of the pump power loss contribution to maintain the operating current below the mass transfer limiting current

The limiting current density ($i_{\lim}$) of a cell, for the case where one of the reactants is limiting, can be written as follows:

$$i_{\lim} = n * F * k_m * C_{bulk} \qquad [9]$$

To have the operating current at 90% galvanic efficiency lower than the mass transfer limiting current:

$$i_{0.9} < i_{\lim} \quad [10]$$

$$0.1\frac{OCV}{ASR} < n * F * k_m * C_{bulk} \quad [11]$$

$$k_m > 0.1\frac{OCV}{n*F*ASR*C_{bulk}} \quad [12]$$

Using Eq. 12, a minimum bound for k_m can be found. k_m is the velocity-dependent mass transfer coefficient, which is affected by electrode pore structure and the flow field design. For each specific electrode under study, experimental and analytical techniques should be employed to find the minimum velocity needed to achieve the desired k_m. To find the pressure drop:

$$\Delta p_{stack} = \frac{\mu v L_e}{K} \quad [13]$$

where μ is the viscosity, L_e is length of the electrode in the direction of electrolyte flow, μ is the viscosity and K is the permeability of the porous electrode, which can be calculated by the Kozenye-Carman equation:

$$K = \frac{d_f^2 * \epsilon^3}{16 * k_{kc} * (1-\epsilon)^2} \quad [14]$$

where d_f is the fibre diameter, k_{kc} is the Kozenye-Carman constant and ϵ is the porosity of the porous electrode. In the calculations done in the manuscript, constants are $\mu = 4.928 * 10^{-3}$ Pa.s, L_e= 0.1 m, $d_f = 1.76 * 10^{-5}$ m, $\epsilon = 0.93$, $k_{kc} = 4.28$.

From the pressure loss, the pump power can be calculated:

$$P_{pump} = \sum_{i=pos,neg} Q_i \Delta p_i / \eta_{pump} \quad [15]$$

Where we assumed a pump efficiency of $\eta_{pump} = 0.85$.